

TOPOLOGICAL MATTER

Quantum anomalous Hall effect in intrinsic magnetic topological insulator MnBi_2Te_4

Yujun Deng^{1,2*}, Yijun Yu^{1,2*}, Meng Zhu Shi^{3*}, Zhongxun Guo^{1,2}, Zihan Xu⁴, Jing Wang^{1,2†}, Xian Hui Chen^{3†}, Yuanbo Zhang^{1,2†}

In a magnetic topological insulator, nontrivial band topology combines with magnetic order to produce exotic states of matter, such as quantum anomalous Hall (QAH) insulators and axion insulators. In this work, we probe quantum transport in MnBi_2Te_4 thin flakes—a topological insulator with intrinsic magnetic order. In this layered van der Waals crystal, the ferromagnetic layers couple antiparallel to each other; atomically thin MnBi_2Te_4 , however, becomes ferromagnetic when the sample has an odd number of septuple layers. We observe a zero-field QAH effect in a five-septuple-layer specimen at 1.4 kelvin, and an external magnetic field further raises the quantization temperature to 6.5 kelvin by aligning all layers ferromagnetically. The results establish MnBi_2Te_4 as an ideal arena for further exploring various topological phenomena with a spontaneously broken time-reversal symmetry.

A distinct feature that is common to all topological materials is the presence of topologically protected quantum states that are robust against local perturbations (1–4). For example, in a topological insulator (TI) such as Bi_2Te_3 , the bulk band topology guarantees the existence of two-dimensional (2D) surface states with gapless Dirac dispersion (5, 6). Introducing magnetism into the initially time-reversal invariant TIs induces profound changes in their electronic structures. Specifically, the long-range magnetic order breaks the time-reversal symmetry and causes an exchange gap in the gapless Dirac dispersion of the surface states (2, 7). The gap opening is accompanied by the emergence of a chiral edge mode that is predicted to give rise to a quantum anomalous Hall (QAH) effect when the Fermi level is situated inside of the exchange gap (2, 8–10). The dissipationless QAH edge channel, combined with the spin-momentum locking that is inherent in topological materials, may lead to advances in device concepts for topological electronic applications (11).

The experimental observation of the QAH effect in chromium-doped $(\text{Bi}, \text{Sb})_2\text{Te}_3$ (10, 12–14) required precise control of the ratio of the multiple elements in this nonstoichiometric material. However, the fine-tuning needed to reconcile conflicting demands—i.e., large mag-

nitization and low initial carrier doping—poses a challenge for material growth, and the randomly distributed magnetic dopants act as impurities that limit the quality of the magnetic TIs. As a result, the exact quantization of the anomalous Hall effect appears only at low temperatures, up to $T = 2$ K (in the penta-layer sandwich structure of topological insulators) (15), which is far below the Curie temperature (a few tens of kelvin) and the exchange gap (hundreds of kelvin) (16) in the material. Further exploration of rich topological phenomena and their potential applications calls for intrinsic magnetic TIs—stoichiometric TIs with an innate magnetic order—so that topological effects can be studied in pristine crystals.

In this work, we probe the quantum transport in atomically thin flakes of intrinsic magnetic TI MnBi_2Te_4 . MnBi_2Te_4 is a layered ternary tetradymite compound that consists of Te-Bi-Te-Mn-Te-Bi-Te septuple layers (SLs, or “layers” hereafter), so the material can be viewed as layered TI Bi_2Te_3 with each of its Te-Bi-Te-Bi-Te quintuple layers intercalated by an additional Mn-Te bilayer (inset of Fig. 1C). The resultant MnBi_2Te_4 crystal remains a TI but now becomes intrinsically magnetic (17–21). The magnetism originates from the Mn^{2+} ions in the crystal, which have a high spin of $S = 5/2$ and a large magnetic moment of $\sim 5\mu_B$ (where μ_B is the Bohr magneton) (17, 18, 20, 22). Below a Neel temperature of $T_N = 25$ K, the spins couple ferromagnetically in each SL with an out-of-plane easy axis, but adjacent SLs couple antiparallel to each other. Bulk MnBi_2Te_4 is, therefore, an antiferromagnet (AFM) (18, 20). In this work, we study thin flakes of MnBi_2Te_4 to minimize the parallel bulk conduction, focusing on MnBi_2Te_4 flakes with an odd number of layers, N . Because the layer magnetization in these odd-layer flakes does not completely cancel, the flakes become ferromagnetic while remaining a TI for $N \geq 3$ (18, 19). Because the SLs are separated by

van der Waals gaps in bulk MnBi_2Te_4 , the extensive arsenal of fabrication techniques developed for 2D materials enables us to obtain few-layer samples that preserve the high quality of the bulk crystals.

We start with high-quality MnBi_2Te_4 single crystals that are grown by flux methods (20, 23), and we obtain atomically thin MnBi_2Te_4 using an Al_2O_3 -assisted exfoliation technique described in (24). Specifically, we first thermally evaporate an Al_2O_3 thin film onto a freshly prepared surface of the bulk crystal. We then lift the Al_2O_3 thin film, along with MnBi_2Te_4 thin flakes cleaved from the bulk, using a thermal release tape. The $\text{Al}_2\text{O}_3/\text{MnBi}_2\text{Te}_4$ stack is subsequently released onto a piece of transparent polydimethylsiloxane (PDMS) and inspected under an optical microscope in transmission mode. Figure 1A displays the optical image of few-layer MnBi_2Te_4 flakes on the Al_2O_3 film attached to PDMS. The transmittance of various numbers of SLs follows the Beer-Lambert law (Fig. 1B), which enables us to precisely determine the layer number. The thin flakes are finally stamped onto a Si wafer covered with 285-nm-thick SiO_2 , followed by deposition of Cr/Au contacts for transport measurements. The degenerately doped Si serves as a backgate, so a voltage bias (V_g) applied between Si and the sample can electrostatically dope electron or hole carriers into MnBi_2Te_4 flakes, depending on the polarity of V_g . The entire device-fabrication process is performed in an argon-filled glove box, where O_2 and H_2O content is kept below 0.5 parts per million to mitigate sample degradation. Figure 1C displays temperature-dependent longitudinal resistance, R_{xx} , of few-layer MnBi_2Te_4 . The AFM transition manifests as a resistance peak at T_N (25). Compared with the bulk value of 25 K, T_N monotonically decreases as the samples become thinner ($T_N = 23$ K in the five-layer sample, 21 K in the four-layer sample, and 18 K in the three-layer sample). We ascribe the suppression of T_N to increased thermal fluctuations as the samples approach the 2D limit. The resistance rises again at the lowest temperatures, probably because of the localization of the carriers in the presence of disorder in the 2D samples.

Few-layer MnBi_2Te_4 flakes exhibit a rich set of magnetic states under a vertical magnetic field. The states manifest as steps in the Hall resistance, R_{yx} , as the magnetic field, $\mu_0 H$, is varied (Fig. 1D). There are three main points to notice in Fig. 1D. First, the three- and five-layer samples (samples 3a and 5a, respectively, as labeled in table S1) become ferromagnetic, whereas the four-layer sample (sample 4a) remains largely antiferromagnetic. The small, residual ferromagnetic response in R_{yx} may come from possible substrate-induced, top-bottom surface asymmetry or from disorders in the sample. Second, juxtaposing the

*State Key Laboratory of Surface Physics and Department of Physics, Fudan University, Shanghai 200438, China.

†Institute for Nanoelectronic Devices and Quantum Computing, Fudan University, Shanghai 200433, China.

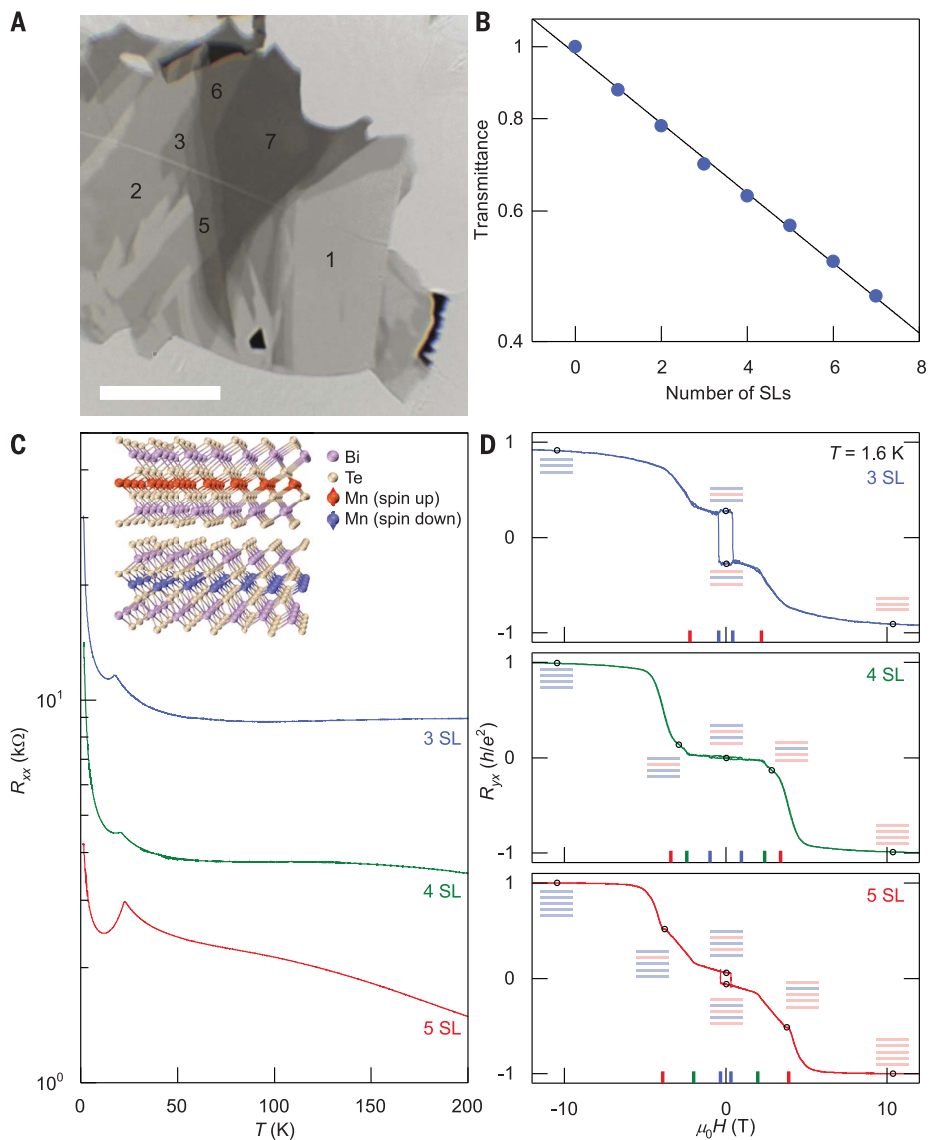
³Hefei National Laboratory for Physical Science at Microscale and Department of Physics, University of Science and Technology of China, and Key Laboratory of Strongly-coupled Quantum Matter Physics, Chinese Academy of Sciences, Hefei, Anhui 230026, China.

⁴SixCarbon Technology, Youmagang Industry Park, Shenzhen 518106, China.

*These authors contributed equally to this work.

†Corresponding author. Email: zhby@fudan.edu.cn (Y.Z.); chenxh@ustc.edu.cn (X.H.C.); wjngphys@fudan.edu.cn (J.W.)

Fig. 1. Fabrication and characterization of few-layer MnBi₂Te₄ devices. (A) Optical image of few-layer flakes of MnBi₂Te₄ cleaved onto thermally evaporated Al₂O₃ thin film (thickness ~70 nm). The MnBi₂Te₄/Al₂O₃ stack is supported on a PDMS substrate. Image was taken in transmission mode. Number of SLs is labeled on selected flakes. Scale bar, 20 μm. (B) Transmittance as a function of the number of SLs. The transmittance (filled circles) follows the Beer-Lambert law (solid line). (C) Temperature-dependent sample resistance of few-layer MnBi₂Te₄. The antiferromagnetic transition manifests as a resistance peak in the three-, four-, and five-layer samples (samples 3a, 4a, and 5a, respectively; see table S1). Inset shows the layered crystal structure of MnBi₂Te₄ in the antiferromagnetic state. The spins of Mn²⁺ ions order ferromagnetically within a layer, whereas neighboring layers couple antiferromagnetically with an out-of-plane magnetocrystalline anisotropy. (D) R_{yx} of the same three-, four-, and five-layer MnBi₂Te₄ samples shown in (C) as a function of external magnetic field applied perpendicularly to the sample plane. Data were obtained at $T = 1.6$ K. All data sets were antisymmetrized to remove the R_{xx} component (23). The external magnetic field flips individual ferromagnetic SLs one SL at a time, and eventually fully polarizes all SLs. The magnetic transitions manifest as jumps in R_{yx} that are marked by colored ticks on the horizontal axes. Cartoons illustrate the magnetic states at representative magnetic fields (marked by open circles). SLs with up or down magnetization are shown in red or blue, respectively. For simplicity, only one of the possible configurations is shown when there are degeneracies; we also ignore magnetic domains that may be present in some of the magnetic states.



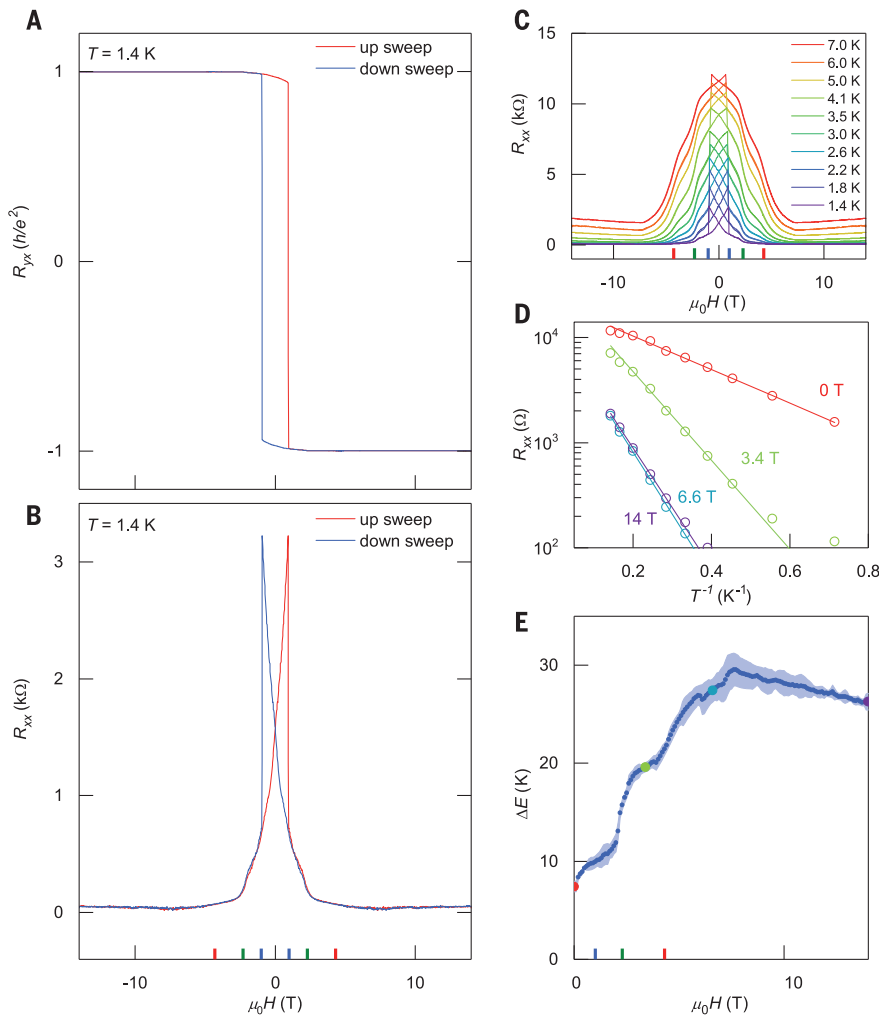
$R_{yx}(\mu_0 H)$ of the three samples provides insight into those magnetic states. $R_{yx}(\mu_0 H)$ in the three-layer sample exhibits three distinct plateaus that indicate three distinct magnetic states marked by empty circles, in contrast with five magnetic states indicated in the four-layer sample and six magnetic states in the five-layer sample. It is evident that the SLs are initially antiferromagnetically coupled, and an increasing external magnetic field flips individual ferromagnetic SLs, one SL at a time, eventually reaching a fully polarized magnetic state above $\mu_0 H \sim 6$ T. These magnetic states are schematically illustrated by the insets in Fig. 1D. The transitions between the states can be described by the Stoner-Wohlfarth model with bipartite AFM (23). The model further points out that each layer flip takes place in two steps via a spin flop transition, where the layer magnetization is free to rotate in directions approximately perpendicular to the easy axis (23). Close examination of the transitions

in $R_{yx}(\mu_0 H)$ reveal signs of such spin flop transitions in sample 5a (fig. S11).

Third, we observe that the anomalous Hall response quantizes to $R_{yx} = h/e^2$ once the external magnetic field fully aligns the magnetization in all SLs (here $h/e^2 = 25.8$ kilohm is the resistance quantum, h is the Planck constant, and e the charge of an electron). The quantization of anomalous R_{yx} is accompanied by a vanishing longitudinal resistance R_{xx} (fig. S3); both features are hallmarks of a QAH state with a dissipationless chiral edge channel. As a voltage, V_g , applied on backgate tunes the charge carrier in the five-layer sample (sample 5c; fig. S5) from the electron to the hole side, the QAH effect does not change sign, in distinct contrast to the carrier-type-dependent ordinary quantum Hall effect that is originated from Landau level (LL) quantization. Furthermore, the quantization is best developed as V_g is tuned to the charge neutrality point (CNP), V_g^{CNP} , where the Fermi level lies in

the middle of the exchange gap (23). The large exchange gap in the fully polarized magnetic state leads to a robust QAH effect at elevated temperatures (fig. S4A). In particular, the anomalous Hall effect in sample 5a remains well quantized ($|R_{xx}|$ stays above $0.97h/e^2$ and R_{xx} below $0.017h/e^2$), under a magnetic field of $\mu_0 H = 12$ T, at temperatures up to $T = 4.5$ K (fig. S4, C and D). Finally, we note that the zero-field anomalous Hall response in typical few-layer samples reaches a substantial fraction of the quantum resistance h/e^2 (up to 27% in sample 3a and 23% in sample 5c) but does not quantize, probably owing to disorder in the samples.

A well-developed QAH effect emerges at zero magnetic field in MnBi₂Te₄ with much-improved sample quality. Figure 2, A and B, displays the R_{yx} and R_{xx} of a high-quality five-layer sample (sample 5b), recorded as a function of a magnetic field at $T = 1.4$ K. The measurements are performed when the backgate is biased at $V_g =$

**Fig. 2. QAH effect in a five-layer $MnBi_2Te_4$ flake.**

(**A** and **B**) Magnetic-field-dependent R_{yx} (**A**) and R_{xx} (**B**) acquired in the five-layer sample 5b at $T = 1.4$ K. R_{yx} and R_{xx} data shown here are antisymmetrized and symmetrized, respectively, to remove the mixing of the two components (23). Up and down sweeps of the magnetic field are shown in red and blue, respectively. R_{yx} reaches $0.97h/e^2$, concomitant with a R_{xx} of $0.061h/e^2$ at $\mu_0 H = 0$ T. These features are unambiguous evidence of zero-field QAH effect. The external magnetic field polarizes the ferromagnetic SLs individually and further improves the QAH quantization; R_{yx} quantizes to $0.998h/e^2$ under magnetic fields above $\mu_0 H \sim 2.5$ T. (**C**) R_{xx} of sample 5b as a function of magnetic field acquired at various temperatures. Data are symmetrized to remove the R_{yx} component. (**D**) Arrhenius plot of R_{xx} as a function of $1/T$ under representative magnetic fields. Solid lines are line fits, the slopes of which yield the energy gap of the thermally activated charge transport. (**E**) Energy gap as a function of magnetic field extracted from fitting the Arrhenius plots exemplified in (D). The shaded region represents the error bound of the energy gap from the line fits. Solid circles highlight the representative gap values obtained from the fittings shown in (D). Colored ticks on the horizontal axes in (B), (C), and (E) mark the locations of magnetic transitions. All data were obtained under a backgate bias of $V_g = -200$ V.

-200 V, close to the CNP. The zero-field remnant anomalous Hall response $R_{yx}|_{\mu_0 H = 0}$ T reaches $0.97h/e^2$, whereas $R_{xx}|_{\mu_0 H = 0}$ T drops to $0.061h/e^2$ at the same time—both are unambiguous evidence of a zero-field QAH effect. The QAH quantization is comparable to that in best magnetically doped TI thin films— $R_{yx} \sim 0.97h/e^2$ and $R_{xx} \sim 0.2h/e^2$, obtained in Cr modulation-doped $(Bi_{1-y}Sb_y)_2Te_3$ at $T = 2$ K (15). We adopt the same $R_{yx} \sim 0.97h/e^2$ quantization criterion as in (15) throughout this work. An external magnetic field further enhances the quantization by aligning the ferromagnetic SLs (such magnetic transitions are visible in R_{xx} as a function of magnetic field as shown in Fig. 2C) and R_{yx} plateaus at $0.998h/e^2$, under magnetic fields above $\mu_0 H \sim 2.5$ T. The ferromagnetic alignment of the SLs also improves the robustness of the QAH effect against thermal fluctuations. We observe that $|R_{yx}|$ stays within 3% of the resistance quantum at temperatures up to $T = 6.5$ K, under a magnetic field of $\mu_0 H = 7.6$ T (fig. S6G).

Temperature-dependent measurements of R_{xx} further reveal the energetics of the QAH

effect in the five-layer flake. Specifically, R_{xx} at $V_g = -200$ V exhibits a thermally activated behavior, $R_{xx} \sim \exp(-\Delta E/2k_B T)$, at elevated temperatures (where k_B is the Boltzmann constant and ΔE the energy gap; Fig. 2C). Line fits to the Arrhenius plots of $\ln R_{xx}$ as a function of $1/T$ yield the energy gap ΔE under various magnetic fields, as shown in Fig. 2, D and E. At zero magnetic field, we obtain an energy gap of $\Delta E = 0.64$ meV, or 7.4 K, which reflects the energy scale of the zero-field QAH effect in sample 5b (Fig. 2D, red line). Such an energy gap is larger than the value found in magnetically doped TI thin films (14), but the energy gap is still much smaller than the exchange gap, E_{ex} , expected in $MnBi_2Te_4$ (19, 20, 23, 25). We emphasize, however, that ΔE does not directly measure the bandgap E_g of the surface states [$E_g = E_{ex}$ in a pristine five-layer $MnBi_2Te_4$; see (23)], but rather characterizes the minimum energy required to excite an electron from the valence to the conduction band. The large difference between ΔE and predicted E_{ex} implies marked surface-band broadening that may be caused by various disorders in the sample. The Fermi

energy, E_F , may not be situated exactly in the middle of the top and bottom surface gap at $V_g = -200$ V. This deviation will also contribute to the difference between the two gap values (23). The broadening may be responsible for the lack of direct observation of the exchange gap in spectroscopy measurements (26–29); there is much room for further increasing the energy scale of the QAH effect in pristine, high-quality $MnBi_2Te_4$.

As an external magnetic field is applied, we observe that ΔE increases in three steps and peaks at 30 ± 2 K when the sample is fully polarized under $\mu_0 H = 7.6$ T. These steps coincide with the magnetic transitions (Fig. 2E). We attribute the stepwise increase in ΔE to the enhanced E_{ex} as the magnetic field aligns the magnetization of the SLs, one layer at a time (23). After the magnetic field fully polarizes the five-layer sample, ΔE diminishes with increasing magnetic field above $\mu_0 H = 7.6$ T (Fig. 2E). The suppression of ΔE stems from the fact that the exchange field (that produces E_{ex}) in $MnBi_2Te_4$ is opposite to the external magnetic field (30). The linear $\Delta E(\mu_0 H)$ in the fully polarized magnetic state exhibits a slope

of -0.74 , whereas an effective model of the surface bands yields an estimate of the g -factor of -2.6 (23). The mismatch between the two values may again come from the possibility that E_F is not situated in the middle of the top and bottom surface gap under a backgate bias of $V_g = -200$ V (23). Finally, we note that the

energy gap stays open from $\mu_0 H = 0$ to 14 T. This provides evidence that the high-field QAH state is adiabatically connected to the zero-field QAH state and that they are, topologically, the same state.

The QAH states gradually evolve into metallic ones as the backgate voltage shifts away

from the CNP. The evolution provides a glimpse into the electronic structure of the surface bands outside of the bandgap. Figure 3A presents R_{yx} of sample 5b as a function of magnetic field under various gate voltages. The four magnetic states on each side of the field sweep are clearly separated by magnetic transitions that

Fig. 3. Gate-tuned QAH effect in a five-layer

MnBi₂Te₄ flake. (A) Magnetic-field-dependent R_{yx} , acquired in sample 5b, under varying gate biases V_g (in 10 V steps). All data were obtained at $T = 1.6$ K. Curves are antisymmetrized to remove the R_{xx} component. Colored ticks on the horizontal axis mark the location of magnetic transitions. (B to D) R_{xx} and R_{yx} as functions of V_g under three representative magnetic fields, $\mu_0 H = 0, 5$, and 14 T. An additional plateau of $R_{yx} = -h/(2e^2)$ emerges at $V_g \sim -25$ V, accompanied by a vanishing R_{xx} (D). The same plateau is also visible in (A) at $\mu_0 H > 10$ T during field sweeps under $V_g = -60$ V. This evidence points to a quantized Hall state with a filling factor $v = -2$. All data were obtained in the same sample 5b, but V_g values do not exactly match those in (A) because of hysteresis during gate sweeps.

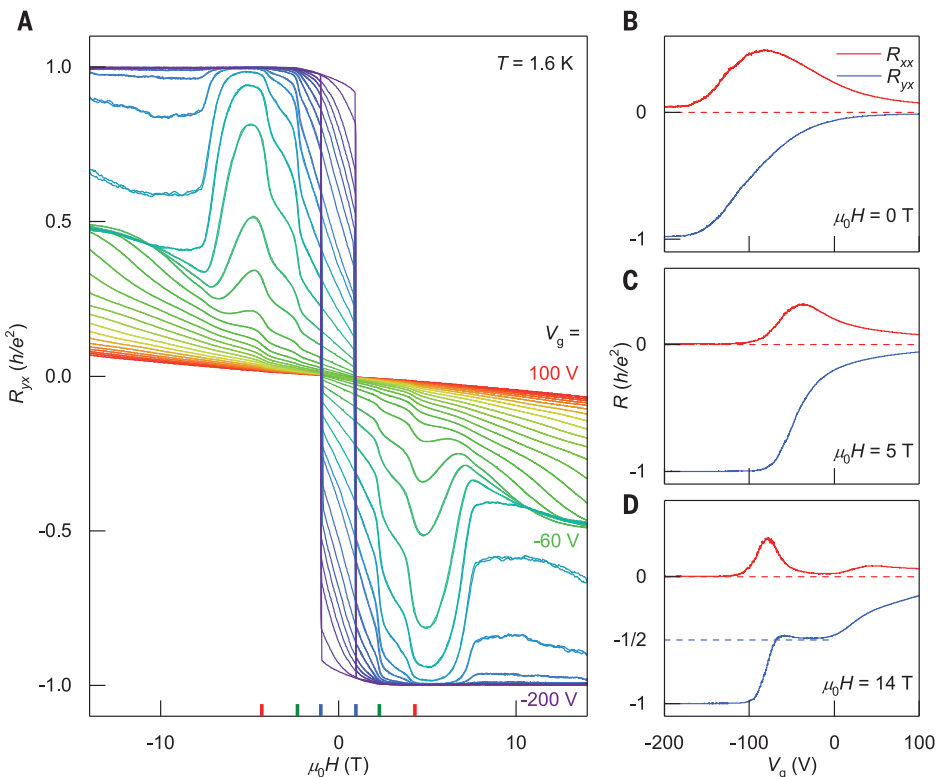
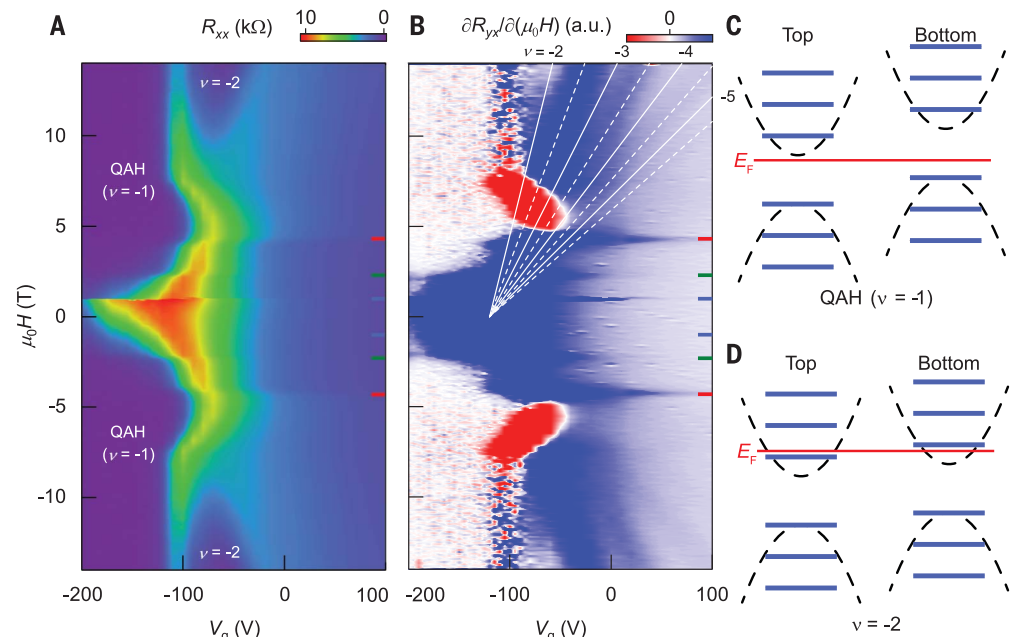


Fig. 4. LLs in a gated five-layer

MnBi₂Te₄ flake. (A and B) R_{xx} (A) and $\partial R_{yx}/\partial \mu_0 H$ (B) plotted as functions of V_g and $\mu_0 H$. $R_{xx}(\partial R_{yx}/\partial \mu_0 H)$ data taken during magnetic field upsweep have been symmetrized (antisymmetrized) with downsweep data. QAH state with $v = -1$ and QH state with $v = -2$ appear in regions with vanishing R_{xx} in (A). $\partial R_{yx}/\partial \mu_0 H$ maxima trace out the centers of half-filled LLs that are marked by broken lines in (B). Solid lines indicate fully filled LLs with filling factors $v = -2, -3, -4$, and -5 . Colored ticks on the right axes mark the magnetic transitions. All data were obtained in sample 5b at $T = 1.6$ K. a.u., arbitrary units. (C and D) Schematic band diagrams for the top and bottom surface states of this five-layer sample. Dashed parabolas denote surface bands under zero magnetic field. The bands collapse into LLs (blue horizontal lines) under an external magnetic field. Red horizontal lines represent Fermi level E_F that is tuned by the backgate in our experiment. (C) and (D) display the band configurations of the observed $v = -1$ and $v = -2$ states, respectively.



manifest as jumps in R_{yx} . Within these magnetic states, the quantized R_{yx} smoothly approaches zero as the backgate dopes electrons into the sample. R_{xx} displays a peak during the process, as is typical for QAH insulator-to-metal transition (10, 12); examples of the transition are shown in Fig. 3, B and C. There is, however, an exception at high magnetic fields: R_{yx} goes through a plateau at $-h/(2e^2)$ during the transition, as shown in Fig. 3D. The same $-h/(2e^2)$ plateau in R_{yx} is also visible at $\mu_0H > 10$ T during field sweeps under $V_g = -60$ V. The plateau is accompanied by a vanishing R_{xx} (23), which signifies the emergence of an additional quantized Hall state apart from the QAH state.

The origin of the additional quantized Hall state becomes clear once we plot R_{xx} and $\partial R_{yx}/\partial \mu_0 H$ as a function of both gate bias, V_g , and magnetic field, $\mu_0 H$ (Fig. 4, A and B; the R_{yx} plot is shown in fig. S8). We observe that $\partial R_{yx}/\partial \mu_0 H$ maxima trace out straight lines that disperse with both V_g and $\mu_0 H$ (Fig. 4B, broken lines), i.e., these states have degeneracies that are proportional to $\mu_0 H$. This behavior is in stark contrast to that of the nondispersive QAH state, but it is characteristic of LLs formed by 2D band electrons; the broken lines traced out by $\partial R_{yx}/\partial \mu_0 H$ maxima mark the center of the half-filled LLs. The slopes of the lines produce the half-integer ratio (1.5:2.5:3.5:4.5), as shown in Fig. 4B. Because the first fully filled LL has a filling factor $v = -2$ [R_{yx} quantizes at $-h/(2e^2)$ for the first fully filled LL], the ratio enables us to uniquely determine the filling factor v of each fully filled state, $v = -2, -3, -4$, or -5 (Fig. 4B, indicated by solid lines between the broken lines). When extrapolated to $\mu_0 H = 0$ T, all the lines converge to $V_g = -120$ V, where the backgate starts to fill the surface band with electrons (Fig. 4A). This is unequivocal evidence that the LLs develop concomitantly with the QAH effect. Such coexistence of LLs and QAH is best exemplified by the $R_{yx} = -h/(2e^2)$ quantization at the first fully filled LL: The LL quantization is responsible for only one of the two edge channels, whereas the QAH effect contributes the other edge channel.

All states observed in this work can be understood from a unified view that separates the filling factor into its two constituents, $v = v_t + v_b$, where $v_{t(b)} = N_{t(b)} - 1/2$ is the filling factor contributed by the top (bottom) surface of the sample. Here, top and bottom are

defined by reference to the substrate underneath the sample; $N_{t(b)}$ is the LL index and $-1/2$ comes from the QAH chiral edge state (31, 32). $(v_t, v_b) = (-1/2, -1/2)$ describes the QAH state when E_F lies inside of the exchange gap on both surfaces (Fig. 4C). As the sample is gated, v jumps by $-1 (+1)$ each time E_F shifts through each electron (hole) level. Because sample 5b is initially electron doped at $V_g = 0$ V, the $v = -2$ state at $V_g = -58$ V will have a large carrier imbalance between the top and bottom surfaces. We determine that the most probable configuration for the $v = -2$ state is $(v_t, v_b) = (-3/2, -1/2)$ as shown in Fig. 4D. Finally, we note that the electrons that form LLs are only a small fraction of the total number of electrons induced by the backgate. Specifically, Hall measurements near zero magnetic field yield a gate efficiency of $5 \times 10^{10} \text{ cm}^{-2} \text{ V}^{-1}$ that agrees reasonably well with the efficiency estimated from the device geometry (fig. S9). The carrier density estimated from the LL degeneracy, however, yields a gate efficiency of only $\sim 10\%$ of this value. The large mismatch has also been observed in gated bismuth chalcogenide TIs (31, 32). Our observation that the $v = -2$ state is well quantized—whereas higher LLs appear only as small oscillations (Fig. 4B, marked by broken lines), possibly weakened by a large parallel conduction—points to bulk bands slightly above the surface-band edge as the probable cause of the discrepancy.

Because MnBi_2Te_4 is a layered material, the techniques developed for 2D materials can be readily applied to MnBi_2Te_4 . We anticipate that van der Waals heterostructures integrating MnBi_2Te_4 with other magnetic or superconducting 2D materials will provide fertile ground for exploring exotic topological quantum phenomena.

REFERENCES AND NOTES

1. F. D. M. Haldane, *Phys. Rev. Lett.* **61**, 2015–2018 (1988).
2. X.-L. Qi, T. L. Hughes, S.-C. Zhang, *Phys. Rev. B* **78**, 195424 (2008).
3. M. Z. Hasan, C. L. Kane, *Rev. Mod. Phys.* **82**, 3045–3067 (2010).
4. X.-L. Qi, S.-C. Zhang, *Rev. Mod. Phys.* **83**, 1057–1110 (2011).
5. H. Zhang et al., *Nat. Phys.* **5**, 438–442 (2009).
6. Y. L. Chen et al., *Science* **325**, 178–181 (2009).
7. Y. L. Chen et al., *Science* **329**, 659–662 (2010).
8. C.-X. Liu, X.-L. Qi, X. Dai, Z. Fang, S.-C. Zhang, *Phys. Rev. Lett.* **101**, 146802 (2008).
9. R. Yu et al., *Science* **329**, 61–64 (2010).
10. C.-Z. Chang et al., *Science* **340**, 167–170 (2013).
11. Y. Tokura, K. Yasuda, A. Tsukazaki, *Nat. Rev. Phys.* **1**, 126–143 (2019).
12. J. G. Checkelsky et al., *Nat. Phys.* **10**, 731–736 (2014).
13. X. Kou et al., *Phys. Rev. Lett.* **113**, 137201 (2014).
14. A. J. Bestwick et al., *Phys. Rev. Lett.* **114**, 187201 (2015).
15. M. Mogi et al., *Appl. Phys. Lett.* **107**, 182401 (2015).
16. I. Lee et al., *Proc. Natl. Acad. Sci. U.S.A.* **112**, 1316–1321 (2015).
17. M. M. Otkrov et al., *2D Mater.* **4**, 025082 (2017).
18. D. Zhang et al., *Phys. Rev. Lett.* **122**, 206401 (2019).
19. J. Li et al., *Sci. Adv.* **5**, eaaw5685 (2019).
20. M. M. Otkrov et al., arXiv:1809.07389 [cond-mat.mtrl-sci] (19 September 2018).
21. Y. Gong et al., *Chin. Phys. Lett.* **36**, 076801 (2019).
22. M. M. Otkrov et al., *Phys. Rev. Lett.* **122**, 107202 (2019).
23. See supplementary materials.
24. Y. Deng et al., *Nature* **563**, 94–99 (2018).
25. S. H. Lee et al., *Phys. Rev. Research* **1**, 012011 (2019).
26. Y.-J. Hao et al., *Phys. Rev. X* **9**, 041038 (2019).
27. Y. J. Chen et al., *Phys. Rev. X* **9**, 041040 (2019).
28. H. Li et al., *Phys. Rev. X* **9**, 041039 (2019).
29. P. Swatek et al., arXiv:1907.09596 [cond-mat.mtrl-sci] (22 July 2019).
30. J. G. Checkelsky, J. Ye, Y. Onose, Y. Iwasa, Y. Tokura, *Nat. Phys.* **8**, 729–733 (2012).
31. Y. Xu et al., *Nat. Phys.* **10**, 956–963 (2014).
32. R. Yoshimi et al., *Nat. Commun.* **6**, 8530 (2015).
33. Y. Deng et al., Harvard Dataverse (2020); <https://doi.org/10.7910/DVN/ZLSDWP>.

ACKNOWLEDGMENTS

We thank X. Jin, Y. Wu, C.-Z. Chang, and S. Guo for helpful discussions. Part of the sample fabrication was conducted at the Nanofabrication Laboratory at Fudan University. **Funding:** Y.D., Y.Y., Z.G., J.W., and Y.Z. acknowledge support from the National Key Research Program of China (grant nos. 2016YFA0300703 and 2018YFA0305600), the NSF of China (grant nos. U1732274, 11527805, 11425415, and 11421404), Shanghai Municipal Science and Technology Commission (grant no. 18JC1410300), and the Strategic Priority Research Program of the Chinese Academy of Sciences (grant no. XDB30000000). Y.Y. also acknowledges support from the China Postdoctoral Science Foundation (grant nos. BX20180076 and 2018M641907). J.W. acknowledges additional support from the NSF of China (grant no. 11774065) and the NSF of Shanghai (grant no. 17ZR1442500). M.Z.S. and X.H.C. acknowledge support from the National Natural Science Foundation of China (grant nos. 11888101 and 11534010), the National Key R&D Program of China (grant nos. 2017YFA0303001 and 2016YFA0300201), the Strategic Priority Research Program of the Chinese Academy of Sciences (grant no. XDB25000000), and the Key Research Program of Frontier Sciences of the Chinese Academy of Sciences (grant no. QYZDY-SSW-SLH021). **Author contributions:** Y.Z., X.H.C., J.W., and Z.X. supervised the project. M.Z.S., Z.X., and X.H.C. grew MnBi_2Te_4 bulk crystals. M.Z.S., Z.G., Y.Y., and Y.D. characterized bulk crystals. Y.D. and Y.Y. fabricated few-layer devices and performed transport measurements. Y.D., Y.Y., Y.Z., J.W., and X.H.C. analyzed the data. J.W. carried out theoretical calculations. Y.D., Y.Y., J.W., and Y.Z. wrote the manuscript with input from all authors. **Competing interests:** None declared. **Data and materials availability:** The data shown in the paper are available at Harvard Dataverse (33).

SUPPLEMENTARY MATERIALS

science.sciencemag.org/content/367/6480/895/suppl/DC1
Materials and Methods
Supplementary Text
Figs. S1 to S12
Table S1
References (34–43)

27 April 2019; accepted 9 January 2020
Published online 23 January 2020
[10.1126/science.aax8156](https://doi.org/10.1126/science.aax8156)